Journal of Materials Chemistry C

Pulsed-flow growth of polar, semipolar and nonpolar AlGaN

Journal:	*Journal of Materials Chemistry C*
Manuscript ID	TC-ART-03-2020-001369.R2
Article Type:	Paper
Date Submitted by the Author:	10-May-2020
Complete List of Authors:	Dinh, Duc; Institute of Materials and Systems for Sustainability, Nagoya University Hu, Nan; Nagoya University Graduate School of Engineering School of Engineering Honda, Yoshio; Institute of Materials and Systems for Sustainability, Nagoya University Amano, Hiroshi; Institute of Materials and Systems for Sustainability, Nagoya University Pristovsek, Markus; Institute of Materials and Systems for Sustainability, Nagoya University

Journal Name

ARTICLE TYPE

Cite this: DOI: 00.0000/xxxxxxxxxx

Pulsed-flow growth of polar, semipolar and nonpolar AlGaN

Duc V. Dinh,*[a] Nan Hu,[b] Yoshio Honda,[a] Hiroshi Amano,[a,c] and Markus Pristovsek[a]

Received Date
Accepted Date

DOI: 00.0000/xxxxxxxxxx

The impacts of pulsed-flow growth on aluminium incorporation in polar (0001), semipolar ($10\bar{1}3$) and ($11\bar{2}2$), as well as nonpolar ($10\bar{1}0$) AlGaN layers have been investigated. The layers were grown simultaneously on differently oriented AlN/sapphire templates by metal-organic vapour phase epitaxy. The AlN mole fraction ($0 < x_{AlN} \leq 0.85$) of the layers was varied by simply changing the supply time of aluminium precursor while keeping nitrogen and gallium precursors constant. Phase separation has been observed for the (0001) and ($11\bar{2}2$) layers by x-ray diffraction, which is attributed to their different surface reconstructions during growth. In contrast, no phase separation has been observed for the ($10\bar{1}0$) and ($10\bar{1}3$) layers, attributed to their stable surfaces during growth. The AlN mole fraction of the differently oriented layers generally follows the order: ($11\bar{2}2$)<(0001)<($10\bar{1}3$)≤($10\bar{1}0$), attributed to their different surface dangling-bond densities. By means of room-temperature luminescence measurements, highly carbon-incorporation has quantitatively been found in all the layers.

1 Introduction

Semipolar and nonpolar oriented III-nitrides have attracted much attention due to reduced built-in fields[1], which significantly increase the wavefunction overlap between electrons and holes resulting in an increased radiative recombination rate in quantum-well structures compared to polar (0001) *c*-plane counterparts. High-efficiency semipolar and nonpolar InGaN-based visible emitters have successfully been demonstrated[2–4]. Additionally, it has been found that due to a very short carrier radiative lifetime, semipolar and nonpolar InGaN-based emitters can be a good candidate for high-speed visible-light-communication systems[5,6]. For semipolar and nonpolar AlGaN-based ultraviolet (UV) emitters, together with an increase in the radiative recombination rate, the dominant transverse magnetic polarization ($E \parallel [0001]$) of the light emission over the whole range of composition also can increase light extraction efficiency[7–9]. These can increase the performance of the UV emitters.

In contrast to InGaN, there are very limited studies about semipolar and nonpolar Al-containing alloys grown on UV-transparent AlN/sapphire templates, e.g., AlGaN[10–16] and AlInN[10,17–19]. Additionally, the lack of available non-*c*-plane AlN bulk substrates hinders studies of Al(Ga,In)N on bulk substrates[9,20–22]. Since 2010, there is only one report about an AlGaN-based UV LED grown on a ($11\bar{2}2$) AlN/sapphire template operating at 307 nm[23]. This is mainly due to very limited studies on growth of non-*c*-plane AlN templates on sapphire[10,16,24–27]. So far, nonpolar ($11\bar{2}0$) *a*-plane AlGaN[10,15] and ($10\bar{1}0$) *m*-plane AlGaN[14,15], as well as semipolar ($10\bar{1}3$)[16] and ($11\bar{2}2$) AlGaN[11,12,15,23] have been grown on different planar sapphire substrates by metal-organic vapour phase epitaxy (MOVPE). For these studies, a continuous growth has commonly been employed, i.e., Al-, Ga- and N-sources were simultaneously introduced during AlGaN epitaxy.

For polar GaN[28] and AlN[29,30] templates grown on sapphire using MOVPE, to improve the crystalline quality and surface morphology of the templates, pulsed-flow MOVPE-growth has been employed. (This growth method will be later abbreviated as pulsed-growth.) Such AlN templates have been used to prepare AlGaN-based UV LEDs operating at 231-261 nm[29]. Pulsed-growth has also been employed for polar quaternary Al(In,Ga)N layers[31] and ternary AlGaN quantum wells[32]. For MOVPE-grown AlGaN, using pulsed-growth also allows to suppress the gas phase pre-reaction between the group III and group V precursors[28,31]. Consequently, this suppression can strongly enhance the aluminium incorporation in AlGaN[12,31]. So far, there is no study about non-*c*-plane AlGaN epitaxy using pulsed-growth.

Recently, it has been found that aluminium incorporation is comparable in (0001), ($10\bar{1}3$), ($11\bar{2}2$), ($11\bar{2}0$) and ($10\bar{1}0$) AlGaN co-loaded layers grown using continuously growth[14–16,19]. This has been attributed to a strong Al-N bond that prevents desorption of gallium atoms incorporated on the different surfaces.

[a] *Institute of Materials and Systems for Sustainability, Nagoya University, Nagoya 464-8601, Japan; E-mail: duc.vn.dinh@gmail.com*
[b] *School of Engineering, Nagoya University, Nagoya 464-8603, Japan.*
[c] *Akasaki Research Center, Nagoya University, Nagoya 464-8603, Japan.*

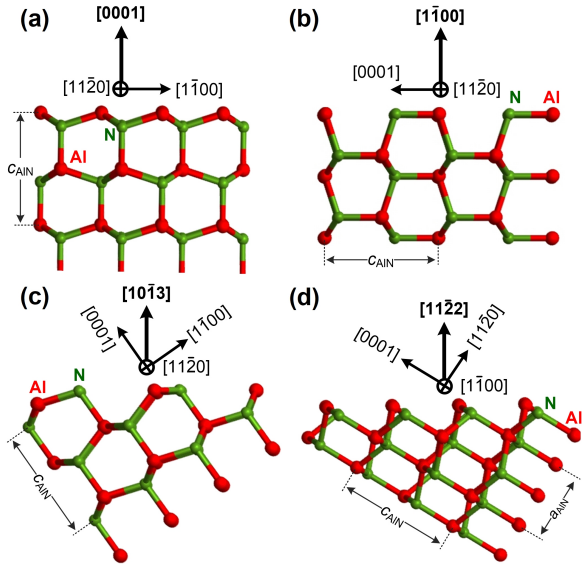

Fig. 1 Schematic illustrations of ideally relaxed Al-polar AlN structures with the (0001) surface (a), (10$\bar{1}$0) surface (b), (10$\bar{1}$3) surface (c), and (11$\bar{2}$2) surface (d) in side view along [11$\bar{2}$0] for (a)-(c) and along [1$\bar{1}$00] for (d).

There is still an open question about the impact of different surface dangling bond densities on aluminium incorporation on differently oriented surfaces. Therefore, to understand this impact, in this paper, we report on pulsed-growth of $Al_xGa_{1-x}N$ layers simultaneously on polar (0001), semipolar (10$\bar{1}$3) and (11$\bar{2}$2), as well as nonpolar (10$\bar{1}$0) AlN/sapphire templates over the entire range of composition.

2 Experimental

Growth was performed in an EpiQuest 3×2-inch close-coupled showerhead MOVPE reactor. Ammonia (NH_3), trimethylgallium (TMGa) and trimethylaluminium (TMAl) were used as precursors. Differently surface-oriented Al-polar AlN templates grown on sapphire substrates were used to grow AlGaN layers, including (0001) AlN ($d\approx350$ nm) on *c*-plane sapphire, (11$\bar{2}$2) AlN ($d\approx1000$ nm) on *m*-plane sapphire, (10$\bar{1}$0) AlN ($d\approx550$ nm) on *m*-plane sapphire, and untwinned (10$\bar{1}$3) AlN ($d\approx350$ nm) on *m*-plane sapphire. Growth parameters of these templates are reported elsewhere[16,26,27]. The total threading dislocation density (TDD) of the (0001) templates is estimated to be about $2\text{-}3\times10^9$ cm^2 by X-ray diffraction (XRD) measurements of the (0002) and (10$\bar{1}$2) AlN X-ray rocking curves. For the non-*c*-plane templates, due to their broad TDD rocking curves[16,26], according to Ref.[33] their TDD is estimated to be in the range of 10^{10} cm^2. Additionally, the basal-stacking fault density of the non-*c*-plane templates is estimated to be in the range of 10^5-10^6 cm^{-1} [26]. It should be noted that similar templates had previously been used to produce continuously grown $Al_yGa_{1-y}N$ layers ($0\leq y\leq1$), which showed clear near-band-edge luminescence at room temperature[15,16]. Fig. 1 shows schematic illustrations of these differently oriented AlN surfaces in side view.

All the 2-inch AlN/sapphire wafers were diced into 1×1 cm^2 pieces. They were then co-loaded into the reactor chamber for

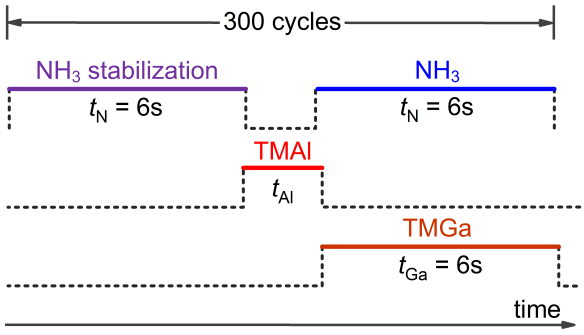

Fig. 2 Representative growth sequence of a cycle using pulsed-flow growth with fixed $t_N = t_{Ga+N} = 6$ s, while $t_{Al} = 1\rightarrow14$ s.

AlGaN epitaxy. Initially, about 50-nm-thick AlN layer was continuously grown on these templates at 1200°C at a reactor pressure of 27 hPa. Afterwards, AlGaN layers were grown on these templates using a pulsed-growth mode at 1100°C at a reactor pressure of 100 hPa in hydrogen (H_2) ambient. The total gas flow rate during AlN and AlGaN epitaxy was kept constant at 15 slm (standard litre per minute). The AlN mole fraction (x_{AlN}) of the layers was varied by alternatively supplying TMAl, TMGa and NH_3 precursors into the reactor. Fig. 2 illustrates a cycle of pulsed-growth including (1) NH_3 stabilization ($t_N = 6$ s, $P_{NH_3} = 3.33$ kPa), (2) only TMAl supply ($t_{Al} = 1\rightarrow14$ s, $P_{TMAl} = 0.61$ Pa) and (3) NH_3 + TMGa supply ($t_{Ga+N} = 6$ s, $P_{NH_3} = 3.33$ kPa and $P_{TMGa} = 0.92$ Pa). The total number of cycles was 300. The nominal layer thickness was of 400-500 nm. For comparison, AlGaN layers were also grown on those differently oriented AlN templates using the continuous growth mode, i.e., all the precursors were simultaneously introduced during AlGaN epitaxy using the same partial pressures mentioned above (V/III ~220).

The structural properties of the AlGaN/AlN samples were characterized using a Malvern PANalytical Empyrean triple-axis high-resolution XRD system equipped with a hybrid monochromator $2\times$Ge(220) Cu asymmetric for $CuK_{\alpha1}$ source ($\lambda = 0.15406$ nm). Reciprocal space maps (RSMs) were measured using the detector in a frame-based (1D) mode. To calculate x_{AlN} of the semipolar and nonpolar AlGaN layers, their lattice constants and distortion angles have been calculated from different symmetric and asymmetric 2θ-ω diffraction peaks, as previously described in details in Refs.[14–16]. For the *c*-plane layers, their lattice constants were calculated from the symmetric (0002) and asymmetric (10$\bar{1}$5) peaks. These peaks were measured using a PIXcel3D-Medipix3 1×1 detector in a scanning mode. The surface morphology of the samples was measured by atomic force microscopy (AFM) in tapping mode (Nanocute, SII NanoTech). The optical properties of the grown samples were investigated by photoluminescence (PL) measurements at room temperature (RT). For RT-PL measurements, the samples were excited by a Krypton Fluoride (KrF) excimer laser (ExciStar XS-200) with excitation wavelength of 248 nm ($E_{ex} = 5$ eV), a spot size of 50×500 μm^2 and a power density of 5.6 kW/cm^2. PL signals were recorded by a high-sensitivity Ocean Optics spectrometer (QE65 Pro).

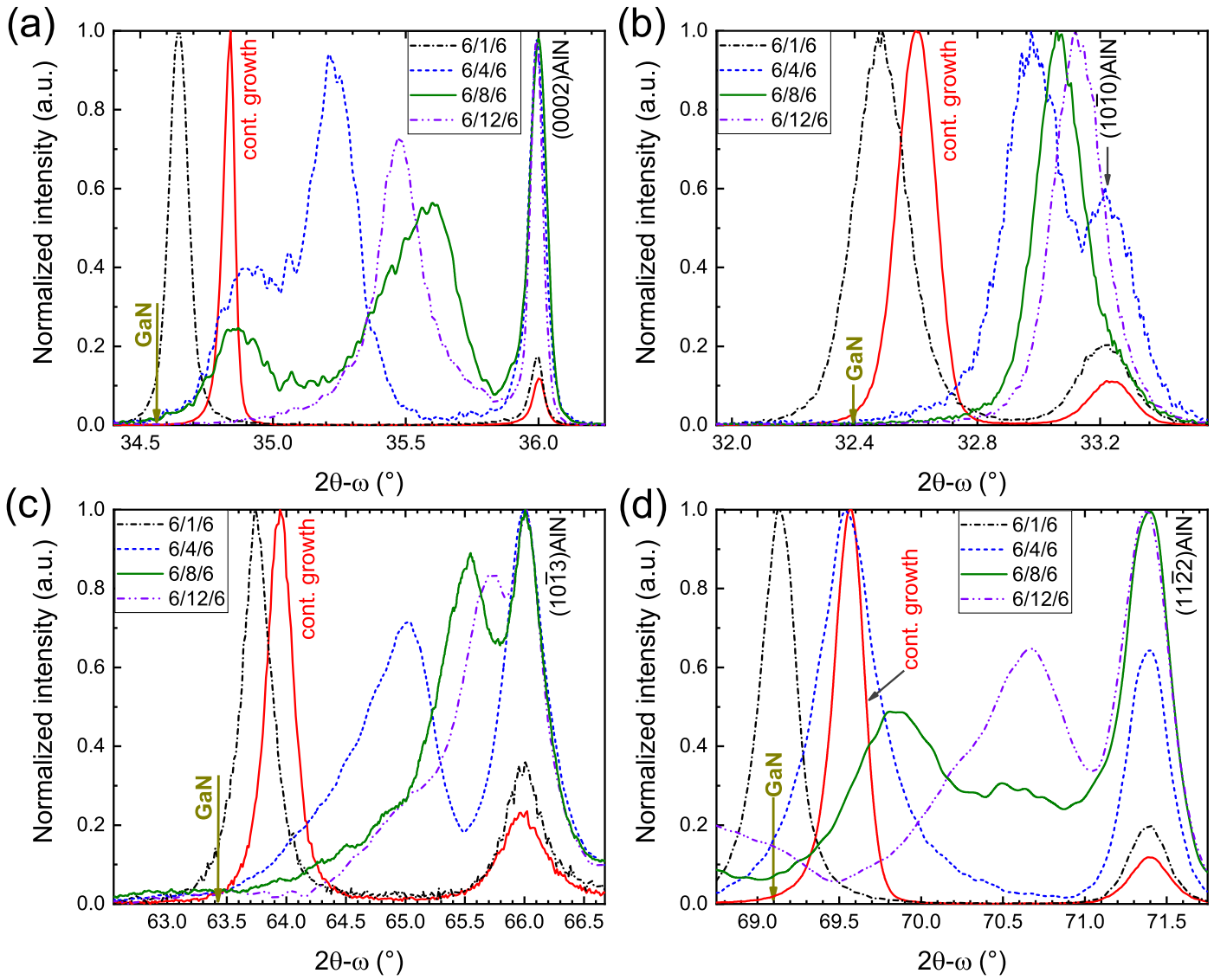

Fig. 3 Symmetric 2θ-ω XRD scans of the (a) (0001), (b) (10$\bar{1}$0), (c) (10$\bar{1}$3) and (d) (11$\bar{2}$2) AlGaN co-loaded layers grown with different $t_N/t_{Al}/t_{Ga+N}$. Scans of the continuously grown layers are also plotted for comparison.

3 Results and Discussion

3.1 Determine aluminium incorporation by XRD

Fig. 3 shows symmetric 2θ-ω XRD scans of the (0001), (10$\bar{1}$3), (11$\bar{2}$2) and (10$\bar{1}$0) AlGaN co-loaded layers grown using the continuous growth method. From compositional calculations based on XRD measurements[14–16], estimated x_{AlN} of these layers has been found to be comparable of 0.22±0.02 (see their x_{AlN} values shown later in Fig. 5). The similar x_{AlN} values of these layers confirm results previously reported for differently oriented AlGaN layers grown with similar growth conditions[14–16].

For all the differently oriented AlGaN layers grown using pulsed-growth with different $t_N/t_{Al}/t_{Ga+N}$, it is clearly seen that simply increasing t_{Al} leads to a shift of symmetric 2θ diffraction peak of AlGaN to a higher value (Fig. 3). This indicates an increase of x_{AlN} in the layers. For the *c*-plane layers grown with $t_{Al} \geq 4$ s (Fig. 3(a)), two diffraction peaks appear, indicating a phase separation in these layers. The dominant (0002) peaks shift to higher 2θ angles with $t_{Al} = 4 \rightarrow 8$ s. For these layers, x_{AlN} of the secondary peak is estimated to be about 0.25±0.05. For the *c*-plane layer grown with $t_{Al} = 12$ s, its phase separation seems to be suppressed as only one peak has been observed. Interestingly, this peak shifts to a lower angle than those of the dominant peak of the layers grown with $t_{Al} = 6$ s and 8 s, indicating a reduced x_{AlN}.

For the (11$\bar{2}$2) layers, a similar phase separations have also been observed for the layers grown with $t_{Al} \geq 4$ s (Fig. 3(d)). However, the dominant (11$\bar{2}$2) peak monotonically shifts to a higher 2θ angle with increasing t_{Al}. This can be clearly seen in RSMs shown in Fig. 4. For the layers grown with $t_{Al} = 4 \rightarrow 8$ s, the secondary peak appears at an angle higher than that of dominant peak. However, for the layers grown with $t_{Al} > 8$ s, their dominant peaks appears at higher angles with very weak intensity of the secondary peaks. Interestingly, for these layers, besides the

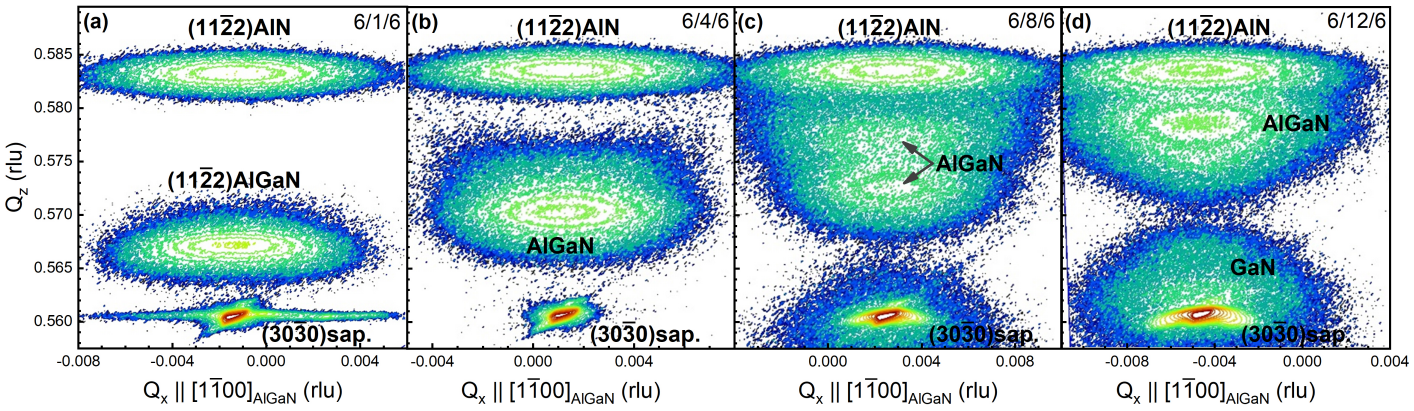

Fig. 4 Symmetric RSM scans of the (11$\bar{2}$2) AlGaN layers grown on (11$\bar{2}$2) AlN/sapphire templates with different $t_N/t_{Al}/t_{Ga+N}$.

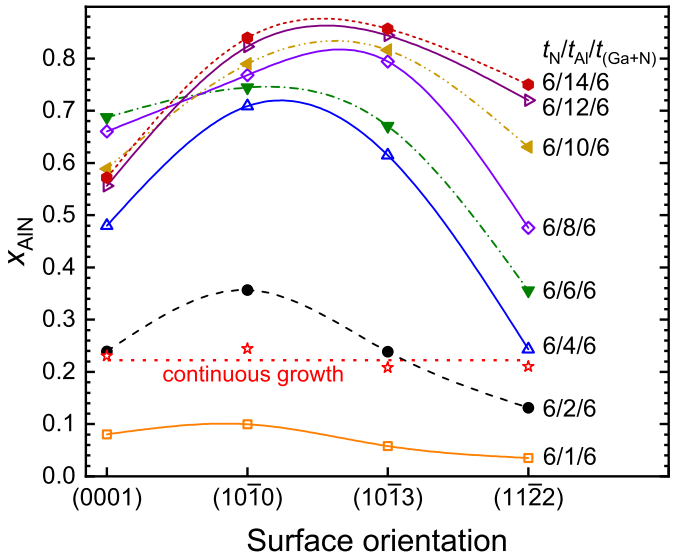

Fig. 5 XRD-estimated x_{AlN} of the (0001), (10$\bar{1}$0), (10$\bar{1}$3), (11$\bar{2}$2) AlGaN co-loaded layers pulsed-grown with different $t_N/t_{Al}/t_{Ga+N}$. Values (☆) estimated for the layers grown using the continuous growth are plotted for comparison.

weak phase separation observed for AlGaN, a very broad peak appears that is close to the (30$\bar{3}$0) sapphire diffraction peak. This can be assigned to the (11$\bar{2}$2) GaN peak (Figs. 3(d) and 4(d)), i.e., some grains of GaN might be formed on top of AlGaN underneath layers. However, such peak is unobservable in the 2θ-ω scans of the other differently oriented co-loaded layers.

In contrast to the *c*-plane and (11$\bar{2}$2) layers, phase separation is unobservable for the (10$\bar{1}$0) layers, as only a single peak has been observed (Fig. 3(b)). Additionally, phase separation is very weak for the (10$\bar{1}$3) layers due to very low intensity of secondary peaks (Fig. 3(c)). Their dominant peak monotonically increases with increasing t_{Al}.

Fig. 5 shows XRD-estimated x_{AlN} of the differently oriented AlGaN layers grown with $t_N/t_{Al}/t_{Ga+N}$. It should be noted that the shown x_{AlN} values of the *c*-plane and (11$\bar{2}$2) layers were estimated from the phases with dominant Al-distributions (Figs. 3(a) and (d)). In contrast to comparable x_{AlN} values of 0.22±0.02 estimated for the continuously grown layers, the pulsed-grown layers have different x_{AlN} with respect to each other. For the pulsed-grown layers with $t_{Al} = 1$ s, their x_{AlN} are smaller than that of the continuously grown layers. However, the layers grown with $t_{Al} \geq 2$ s, their x_{AlN} are comparable (as estimated for the *c*-plane and (10$\bar{1}$3) layers) or even higher (as estimated for the *m*-plane layer) than that of the continuously grown layers, except for the (11$\bar{2}$2) layer. By increasing t_{Al}, x_{AlN} of the pulsed-grown (10$\bar{1}$0) and (10$\bar{1}$3) layers increases considerably, as shown in Figs. 3(b)-(c). The maximum x_{AlN} of the (10$\bar{1}$0) and (10$\bar{1}$3) AlGaN layers is of ~0.85 ($t_{Al} = 14$ s).

For the (11$\bar{2}$2) layers, the maximum x_{AlN} (of the dominant phase) is ~0.75 ($t_{Al} = 14$ s). As previously mentioned, the *c*-plane layers grown with $t_{Al} \geq 10$ s, their (0002) XRD peaks shift to lower diffraction angles, indicating a reduced x_{AlN}. This can be clearly seen in Fig. 5. The x_{AlN} value of the *c*-plane layers reaches a maximum of about 0.67±0.02 at $t_{Al} = 6$ and 8 s, then it reduces to a value of about 0.57±0.02 for the layers grown with longer t_{Al}.

3.2 Surface morphology

Fig. 6 shows 10 μm × 10 μm AFM images of the (0001), (10$\bar{1}$0), (10$\bar{1}$3), (11$\bar{2}$2) AlGaN co-loaded layers pulsed-grown with different $t_N/t_{Al}/t_{Ga+N}$. The surface morphology of the *c*-plane layers grown with $t_{Al} > 1$ s shows different areas separated by boundaries, attributed to the occurrence of their phase separation (Fig 3(a)). Root-mean-square roughness values of these *c*-plane layers have been found to decrease from about 43 nm to 13 nm with $t_{Al} = 1 \rightarrow 12$ s. For the layers grown with $t_{Al} > 8$ s, their morphologies are smoother, likely resulting in their suppressed phase separation.

The non-*c*-plane AlGaN layers show typically undulated surface morphology (with V-shaped patterns), i.e., along [0001]/[11$\bar{2}$0]/[1$\bar{1}$00] for the (10$\bar{1}$0)/(10$\bar{1}$3)/(11$\bar{2}$2) layers, respectively. Such morphology is attributed to anisotropic diffusion lengths of group-III atoms on these surfaces along two in-plane directions[11–14,16–19]. The morphologies of the pulsed-grown (10$\bar{1}$0) and (10$\bar{1}$3) layers are similar to that of continuously grown layers previously reported in Refs.[14,16]. Compared to the morphologies of the (10$\bar{1}$0) and (10$\bar{1}$3) pulsed-grown layers, those of the (11$\bar{2}$2) layers have much larger V-shaped patterns. Additionally, compared to morphology of con-

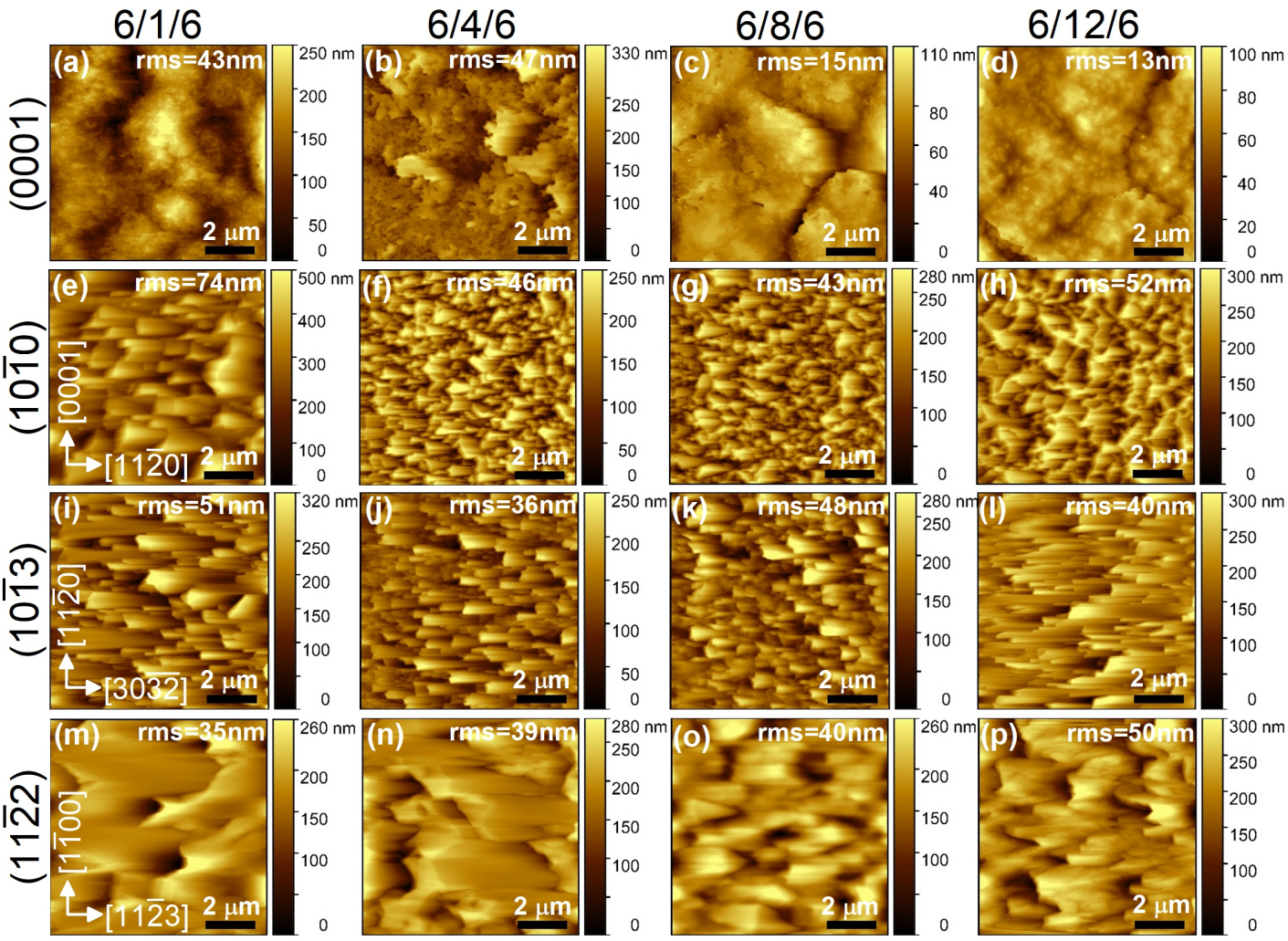

Fig. 6 10 μm × 10 μm AFM images of the (0001), (10$\bar{1}$0), (10$\bar{1}$3), (11$\bar{2}$2) AlGaN co-loaded layers pulsed-grown with different $t_N/t_{Al}/t_{Ga+N}$. Root-mean square (rms) roughness values of these layers are shown for comparison.

tinuously grown (11$\bar{2}$2) AlGaN layers previously reported in the literature[11,12], pattern sizes of the (11$\bar{2}$2) layers studied here are much larger and less undulated. This can be attributed to the pulsed-growth conditions employed here, which resulted in the different surface diffusions and surface reconstructions (discussed later in section 3.4.1). For continuously grown (11$\bar{2}$2) AlGaN layers on GaN microrods on *m*-plane sapphire[34], by using cathodoluminescence hyper-spectral imaging, lower Al incorporations have been found near and around micro-sized V-shaped features compared to feature-free areas. Given the rough morphology of the layers studied here, one might expect similar alloy fluctuations around their surface features.

3.3 Photoluminescence

Fig. 7 shows RT-PL spectra (E_{ex} = 5 eV) of the (0001), (10$\bar{1}$0), (10$\bar{1}$3) and (11$\bar{2}$2) AlGaN co-loaded layers pulsed-grown with $t_N/t_{Al}/t_{Ga+N}$ = 6/8/6. For all the continuously grown layers ($x_{AlN} \approx 0.22 \pm 0.02$), only near-band-edge emission energy has been observed at (3.9±0.1) eV with a full-width at half maximum (Δ_{PL}) of (0.19±0.03) eV. Similar finding has been found for continuously grown layers with different surface orientations previously reported in Refs.[14–16].

From the PL spectra shown in Fig. 7, despite different x_{AlN} of the pulsed-grown layers (Fig. 5), all their spectra show dominant emission energy at about ~3.6-3.9 eV. This dominant emission mainly originates from substitutional carbons on nitrogen sites (C_N), as previously reported for Al(In)N[19,35–37]. The spectrum of the (11$\bar{2}$2) layer shows two peaks at about 3.6 and 3.8 eV (after Gaussian fitting of the corresponding bands), likely related to their phase separation (Fig. 3(d)) that might incorporate different concentrations of impurities. This dominant has also been observed for all the other pulsed-grown samples, generally shifting from ~3.5 to 3.9 eV with increasing x_{AlN} ($\Delta_{PL} \approx (0.20 \pm 0.01) \rightarrow (0.42 \pm 0.13)$ eV). For bulk AlN crystals, it has been found that an increased [C] in AlN shifts the C_N-related emission energy to higher energy regions (e.g., $[C] \approx 2\times10^{17} \rightarrow 2\times10^{19}$ cm^{-3})[35]. This is plausible for the layers studied here, as [C] has previously been found increase with increasing x_{AlN} in AlGaN[38]. The dominant C_N emission observed for the pulsed-grown samples indicates highly C-incorporated into them. This can be explained due to the fact that more C-

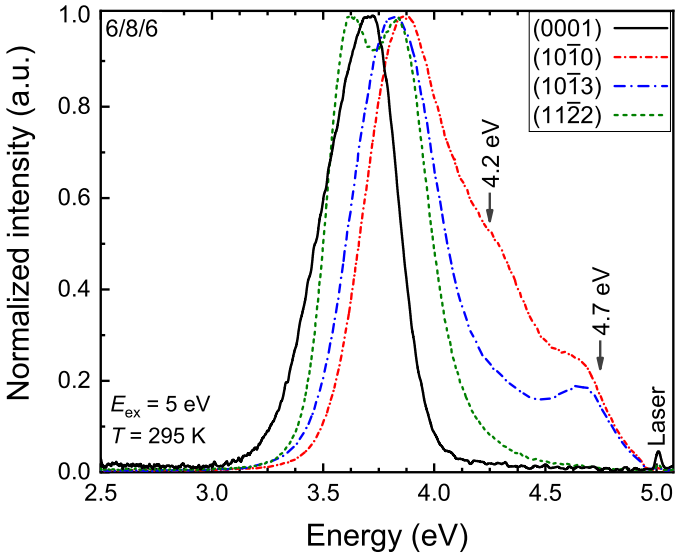

Fig. 7 RT-PL spectra of the (0001), (10$\bar{1}$0), (10$\bar{1}$3) and (11$\bar{2}$2) AlGaN co-loaded layers pulsed-grown with $t_N/t_{Al}/t_{Ga+N} = 6/8/6$.

containing species (e.g., $Al_xC_yH_z$ and $Al_xC_yN_z$ [38–40]) will be easily incorporated on the exposed surfaces during TMAl supply without NH_3 (i.e., V/III = 0).

Additionally, the PL shoulders at ~4.2 eV and ~4.7 eV (after Gaussian fitting of the corresponding bands) observed for the (10$\bar{1}$0) and (10$\bar{1}$3) layers ($x_{AlN} \approx 0.76$-0.78) are attributed to acceptor C_N^- and nitrogen vacancies (V_N), respectively[37].

3.4 Discussion

3.4.1 Surface reconstructions

It is well-known that TMAl:NH_3 pre-reactions strongly occur when introducing TMAl and NH_3 simultaneously during AlGaN epitaxy in MOVPE, limiting the Al incorporation[12,31]. Pulsed-growth can suppress these pre-reactions, resulting in an enhanced Al-incorporation as observed for the AlGaN layers studied here (Fig. 5). During the pulsed-growth, as TMAl was introduced with different t_{Al} without NH_3, the surface stoichiometry of the layers was actually changed from Al-poor to Al-rich conditions. This might lead to different surface reconstructions, causing a formation of coexistence areas with different x_{AlN} (i.e., phase separation) in one layer.

During MOVPE growth of AlGaN in H_2 ambient (i.e., using H_2 carrier gas), the layer surfaces interact with H-rich ambient conditions. Due to stronger N-H bond energy (~3.5 eV) than those of Al-H (~3 eV) and Ga-H (~2.8 eV)[41], H atoms easily terminate the topmost N atoms on the Al(Ga)N surfaces. There are few reports for reconstructions of differently oriented AlN and GaN during MOVPE growth, including (0001)[42,43], (11$\bar{2}$2)[42,44,45], as well as (10$\bar{1}$0)[42,46]. Additionally, for GaN MOVPE-grown at 1100°C (i.e., the temperature used for AlGaN epitaxy in this study), only GaN desorption happens[42]. Therefore, surface reconstructions of the AlGaN layers studied here are mainly governed by the stability of AlN surfaces.

For MOVPE-grown (0001) AlN layers grown in H_2 ambient at 1050°C[47], by varying P_{NH_3} (i.e., V/III ratios) from high → low → without NH_3, surface reconstruction has been found to likely change from 2×2-N → $\sqrt{3}\times\sqrt{3}$-$R30°$ → (1×1)-Al. These various surface reconstructions of the (0001) AlN surface have been linked well to their stability as a function of the Al and Ga chemical potentials[42].

For the (10$\bar{1}$0) GaN and AlN surfaces, by using first-principles calculations, their ideal 1×1 symmetry has been found to be stable over the thermodynamically allowed range, irrespective of N-rich or H-rich conditions used at 1100°C[42,46]. The (10$\bar{1}$3) GaN surface has been found to have a remarkable morphological stability, stabilizing a metallic structure (Ga adlayer) over the entire range of the Ga chemical potential in N-rich conditions[48]. So far, no calculations for the (10$\bar{1}$3) AlN surface have been studied. However, as shown in Figs. 1(c)-(d), the (10$\bar{1}$3) AlN surface exhibits a kind of similar atomic arrangement to the (10$\bar{1}$0) AlN surface with the topmost N and Al atoms. Thus, one can expect that their surface reconstructions should show the same behaviours over the chemical potential range. Therefore, the (10$\bar{1}$3) AlN surface can also be considered as a stable surface, i.e., similar to the GaN surfaces. For the (11$\bar{2}$2) AlN surface in H-rich conditions, three different reconstructions have been found at 1100°C with increasing Al pressure, including c(2×2) with H atoms [Al_{adatom}-H+N-AlH_2], 2×2 8N-6Al and c(2×2)-Al adatom[45].

Conclusively, with the above discussion, for the pulsed-grown (10$\bar{1}$0) and (10$\bar{1}$3) layers, their stable surfaces are consistent with the unchanged surface morphology of the AlGaN grown layers as shown in Figs. 6(a)-(h), consistent with the absence of phase separation in these layers as shown in Figs. 3(c)-(d). For the pulsed-grown (0001) and (11$\bar{2}$2) AlGaN layers studied here, their different surface morphologies (Figs. 6(i)-(p)) can be attributed to different surface reconstructions during growth, resulting in their phase separation as observed by XRD (Figs. 3(a)-(b)). Further investigations are under going to find out if such phase separation caused by different stacked layers or localized areas.

3.4.2 Surface dangling bonds

The differences in x_{AlN} of the pulsed-grown layers can also be attributed to differences in dangling-bond (db) density on their differently oriented surfaces. As shown in Fig. 1, the ideal (0001) and (11$\bar{2}$2) AlN surfaces both have the topmost Al atoms, while the ideal (10$\bar{1}$3) and (10$\bar{1}$0) AlN surfaces are terminated with both N and Al atoms. However, on the (10$\bar{1}$3) surface, each Al atom has one db, while each N atom has one or two dbs. In contrast, on the (10$\bar{1}$0) surface, each Al and each N atoms have only one db. Table 1 shows the surface N- and (Al,Ga)-db densities (D_N, $D_{Al,Ga}$) calculated for different AlN and GaN surfaces. For these calculations, lattice constants of unstrained AlN and GaN have been used[49].

During the AlGaN pulsed-growth, after introducing TMAl, Al-N bonds will be formed first. The higher number of N-sites exists on a surface, the higher number of Al-N bonds can be formed. Ga-N bonds can only be formed at the residual N-sites after introducing TMGa (with NH_3). Consequently, the higher D_N on the (10$\bar{1}$0) and (10$\bar{1}$3) surfaces results in their higher aluminium incorporations than those on the (0001) and (11$\bar{2}$2) surfaces.

Table 1 Lattice constants of unstrained AlN and GaN [49] used to calculate surface dangling-bond densities ($D^{AlN,GaN}$) of Al, Ga, and N atoms on different ideal AlN and GaN surfaces.

Materials	Lattice constants (angstrom)			
AlN	$a_0 = 3.111\ 97$; $c_0 = 4.980\ 89$			
GaN	$a_0 = 3.189\ 40$; $c_0 = 5.186\ 14$			
Surface orientations	Dangling-bond density (nm^{-2})			
	D_{Al}^{AlN}	D_{N}^{AlN}	D_{Ga}^{GaN}	D_{N}^{GaN}
(0001)	11.90	-	11.35	-
$(10\bar{1}0)$	6.45	6.45	6.05	6.05
$(10\bar{1}3)$	10.15	15.23	9.62	14.43
$(11\bar{2}2)$	18.95	-	17.84	-

As shown in Table 1, $D_{N}^{Al(Ga)N}$ of the $(10\bar{1}3)$ surface is higher than that of the $(10\bar{1}0)$ surface. Therefore, Ga atoms will have more chance to incorporate on the $(10\bar{1}3)$ surface than on the $(10\bar{1}0)$ surface. This explains why x_{AlN} of the grown $(10\bar{1}3)$ AlGaN layers is lower than that of the $(10\bar{1}0)$ co-loaded layers for $t_{Al} = 1 \rightarrow 6$ s. Further increasing t_{Al} can increase the number of Al-N bonds, resulting in an increase of x_{AlN}. However, x_{AlN} values of the $(10\bar{1}0)$ layers grown with $t_{Al} = 8 \rightarrow 14$ s are slightly lower than that of the $(10\bar{1}3)$ layers ($\Delta x \leq 0.04$). As mentioned above, the $(10\bar{1}0)$ AlGaN surface is very stable, i.e., Al adlayers cannot be formed on this surface [42,46]. This means that for $t_{Al} \geq 8$ s, instead of forming Al adlayers on the $(10\bar{1}0)$ surface, abundant Al atoms will be desorpted. In contrast, due to the higher $D_{N}^{Al(Ga)N}$ of the $(10\bar{1}3)$ surface, the number of Al-N bonds still keeps increasing with t_{Al}, resulting in higher t_{Al} of the $(10\bar{1}3)$ layers with $t_{Al} \geq 8$ s.

For the *c*-plane and $(11\bar{2}2)$ layers, due to their phase separation, it is difficult to compare their x_{AlN}. However, the trend of lower x_{AlN} with higher db density is evident. Furthermore, these surfaces only have metal dangling bonds, and thus pick up N atoms easily. Since the bond energy of Ga-N (8.92 eV/atom [50]) is lower than that of Al-N (11.52 eV/atom [50]), Al wants to exchange with Ga on the surface until the accumulated strain makes this process unfavourable. Hence, on these two different surfaces, Al atoms are "consuming" the previous GaN layer, and thus form an Al-poor AlGaN layer first until limited by further Al supply and strain.

4 Conclusions

Growth of $Al_xGa_{1-x}N$ layers simultaneously on polar (0001), semipolar $(10\bar{1}3)$ and $(11\bar{2}2)$, as well as nonpolar $(10\bar{1}0)$ AlN templates has been investigated by metal-organic vapour phase epitaxy. A pulsed-flow growth mode was used to vary the AlN mole fraction ($0 < x_{AlN} \leq 0.85$) in the layers. Phase separation has been observed for the (0001) and $(11\bar{2}2)$ layers, attributed to their different surface reconstructions during growth. In contrast, no phase separation has been observed for the $(10\bar{1}0)$ and $(10\bar{1}3)$ layers, attributed to their stable surfaces during growth. The AlN mole fraction of the differently oriented layers generally follows the order: $(11\bar{2}2) < (0001) < (10\bar{1}3) \leq (10\bar{1}0)$. This has been attributed to their different surface dangling bonds, from which the surface with higher cation dangling bond density (i.e., $(10\bar{1}3)$ and $(10\bar{1}0)$) incorporated more aluminium during pulsed-growth. For the (0001) and $(11\bar{2}2)$ layers, the trend of lower x_{AlN} with higher anion dangling bond density has also been found, which might be attributed to different bond energies between Ga-N and Al-N, as well as surface relaxation. By means of room-temperature luminescence measurements, highly carbon-incorporation has quantitatively been found in the layers, whose emission energy slightly increases from ~3.6 to 3.9 eV with increasing x_{AlN}.

Conflicts of interest

There are no conflicts to declare.

Acknowledgements

The authors gratefully acknowledge the supports from the Program for Promoting the Enhancement of Research Universities. This work was also partially supported by Strategic International Collaborative Research Program (SICORP) of Japan Science and Technology Agency (JST), MOST-SKRDP (2016YFE0118400).

References

1 T. Takeuchi, S. Sota, M. Katsuragawa, M. Komori, H. Takeuchi, H. Amano and I. Akasaki, *Jpn. J. Appl. Phys.*, 1997, **36**, L382.
2 M. Funato, M. Ueda, Y. Kawakami, Y. Narukawa, T. Kosugi, M. Takahashi and T. Mukai, *Jpn. J. Appl. Phys.*, 2006, **45**, L659–L662.
3 S. Takagi, Y. Enya, T. Kyono, M. Adachi, Y. Yoshizumi, T. Sumitomo, Y. Yamanaka, T. Kumano, S. Tokuyama, K. Sumiyoshi, N. Saga, M. Ueno, K. Katayama, T. Ikegami, T. Nakamura, K. Yanashima, H. Nakajima, K. Tasai, K. Naganuma, N. Fuutagawa, Y. Takiguchi, T. Hamaguchi and M. Ikeda, *Appl. Phys Express*, 2012, **5**, 082102.
4 D. F. Feezell, J. S. Speck, S. P. DenBaars and S. Nakamura, *J. Disp. Technol.*, 2013, **9**, 190–198.
5 D. V. Dinh, Z. Quan, B. Roycroft, P. J. Parbrook and B. Corbett, *Opt. Lett.*, 2016, **41**, 5752–5755.
6 M. Monavarian, A. Rashidi, A. A. Aragon, S. H. Oh, A. K. Rishinaramangalam, S. P. DenBaars and D. Feezell, *Appl. Phys. Lett.*, 2018, **112**, 041104.
7 H. Kawanishi, M. Senuma, M. Yamamoto, E. Niikura and T. Nukui, *Appl. Phys. Lett.*, 2006, **89**, 081121.
8 R. G. Banal, M. Funato and Y. Kawakami, *Phys. Rev. B*, 2009, **79**, 121308.
9 M. Funato, K. Matsuda, R. G. Banal, R. Ishii and Y. Kawakami, *Phys. Rev. B*, 2013, **87**, 041306.
10 M. R. Laskar, T. Ganguli, A. A. Rahman, A. P. Shah, M. R. Gokhale and A. Bhattacharya, *Phys. Status Solidi (RRL)*, 2010, **4**, 163–165.
11 J. Stellmach, F. Mehnke, M. Frentrup, C. Reich, J. Schlegel, M. Pristovsek, T. Wernicke and M. Kneissl, *J. Cryst. Growth*, 2013, **367**, 42–47.
12 D. V. Dinh, S. N. Alam and P. J. Parbrook, *J. Cryst. Growth*, 2016, **435**, 12–18.

13 D. V. Dinh, P. Pampili and P. J. Parbrook, *J. Cryst. Growth*, 2016, **451**, 181–187.

14 D. V. Dinh, H. Amano and M. Pristovsek, *J. Cryst. Growth*, 2019, **512**, 100–104.

15 D. V. Dinh, N. Hu, Y. Honda, H. Amano and M. Pristovsek, *Sci. Rep.*, 2019, **9**, 1–7.

16 D. V. Dinh, N. Hu, H. Amano, Y. Honda and M. Pristovsek, *Semicond. Sci. Technol.*, 2019, **34**, 125012.

17 N. Hatui, M. Frentrup, A. A. Rahman, A. Kadir, S. Subramanian, M. Kneissl and A. Bhattacharya, *J. Cryst. Growth*, 2015, **411**, 106–109.

18 D. V. Dinh, H. Li and P. J. Parbrook, *Phys. Status solidi B*, 2015, **253**, 99–104.

19 D. V. Dinh, N. Hu, Y. Honda, H. Amano and M. Pristovsek, *Semicond. Sci. Technol.*, 2020, **35**, 035004.

20 S. Ichikawa, Y. Iwata, M. Funato, S. Nagata and Y. Kawakami, *Appl. Phys. Lett.*, 2014, **104**, 252102–1–4.

21 R. G. Banal, Y. Taniyasu and H. Yamamoto, *Appl. Phys. Lett.*, 2014, **105**, 053104.

22 T. Wunderer, Z. Yang, M. Feneberg, M. Batres, M. Teepe and N. Johnson, *Appl. Phys. Lett.*, 2017, **111**, 111101–1–3.

23 K. Balakrishnan, V. Adivarahan, Q. Fareed, M. Lachab, B. Zhang and A. Khan, *Jpn. J. Appl. Phys.*, 2010, **49**, 040206.

24 J. Stellmach, M. Frentrup, F. Mehnke, M. Pristovsek, T. Wernicke and M. Kneissl, *J. Cryst. Growth*, 2012, **355**, 59–62.

25 D. V. Dinh, M. Conroy, V. Z. Zubialevich, N. Petkov, J. D. Holmes and P. J. Parbrook, *J. Cryst. Growth*, 2015, **414**, 94–99.

26 D. V. Dinh, H. Amano and M. Pristovsek, *J. Cryst. Growth*, 2018, **502**, 14–18.

27 N. Hu, D. V. Dinh, M. Pristovsek, Y. Honda and H. Amano, *J. Cryst. Growth*, 2019, **507**, 205–208.

28 M. Asif Khan, R. A. Skogman, J. M. Van Hove, D. T. Olson and J. N. Kuznia, *Appl. Phys. Lett.*, 1992, **60**, 1366–1368.

29 H. Hirayama, T. Yatabe, N. Noguchi, T. Ohashi and N. Kamata, *Appl. Phys. Lett.*, 2007, **91**, 071901.

30 H. Kröncke, S. Figge, T. Aschenbrenner and D. Hommel, *J. Cryst. Growth*, 2013, **381**, 100–106.

31 J. Zhang, E. Kuokstis, Q. Fareed, H. Wang, J. Yang, G. Simin, M. A. Khan, R. Gaska and M. Shur, *Appl. Phys. Lett.*, 2001, **79**, 925–927.

32 J. P. Zhang, M. A. Khan, W. H. Sun, H. M. Wang, C. Q. Chen, Q. Fareed, E. Kuokstis and J. W. Yang, *Appl. Phys. Lett.*, 2002, **81**, 4392–4394.

33 M. A. Moram, C. F. Johnston, M. J. Kappers and C. J. Humphreys, *J. Cryst. Growth*, 2009, **311**, 3239–3242.

34 J. Bruckbauer, Z. Li, G. Naresh-Kumar, M. Warzecha, P. R. Edwards, L. Jiu, Y. Gong, J. Bai, T. Wang, C. Trager-Cowan and R. W. Martin, *Sci. Rep.*, 2017, **7**, 10804.

35 R. Collazo, J. Xie, B. E. Gaddy, Z. Bryan, R. Kirste, M. Hoffmann, R. Dalmau, B. Moody, Y. Kumagai, T. Nagashima, Y. Kubota, T. Kinoshita, A. Koukitu, D. L. Irving and Z. Sitar, *Appl. Phys. Lett.*, 2012, **100**, 191914–1–5.

36 B. E. Gaddy, Z. Bryan, I. Bryan, R. Kirste, J. Xie, R. Dalmau, B. Moody, Y. Kumagai, T. Nagashima, Y. Kubota, T. Kinoshita, A. Koukitu, Z. Sitar, R. Collazo and D. L. Irving, *Appl. Phys. Lett.*, 2013, **103**, 161901.

37 D. Alden, J. S. Harris, Z. Bryan, J. N. Baker, P. Reddy, S. Mita, G. Callsen, A. Hoffmann, D. L. Irving, R. Collazo and Z. Sitar, *Phys. Rev. Appl.*, 2018, **9**, 054036.

38 G. Parish, S. Keller, S. P. Denbaars and U. K. Mishra, *J. Electron. Mater.*, 2000, **29**, 15–20.

39 N. Suzuki, C. Anayama, K. Masu, K. Tsubouchi and N. Mikoshiba, *Jpn. J. Appl. Phys.*, 1986, **25**, 1236–1242.

40 J. Leitner, J. Stejskal and Z. Sofer, *Phys. Status Solidi C*, 2005, **2**, 2504–2507.

41 Y.-R. Luo, *Comprehensive handbook of chemical bond energies*, CRC Press, 2007.

42 Y. Kangawa, T. Akiyama, T. Ito, K. Shiraishi and T. Nakayama, *Materials*, 2013, **6**, 3309–3360.

43 T. Akiyama, D. Obara, K. Nakamura and T. Ito, *Jpn. J. Appl. Phys.*, 2011, **51**, 018001.

44 E. Kalesaki, L. Lymperakis, J. Kioseoglou, J. Neugebauer, Th. Karakostas and Ph. Komninou, *J. Appl. Phys.*, 2012, **112**, 033510.

45 Y. Seta, T. Akiyama, A. M. Pradipto, K. Nakamura and T. Ito, *J. Cryst. Growth*, 2019, **510**, 7–12.

46 T. Akiyama, Y. Saito, K. Nakamura and T. Ito, *Jpn. J. Appl. Phys.*, 2012, **51**, 048002.

47 M. Pristovsek, K. Bellman, F. Mehnke, J. Stellmach, T. Wernicke and M. Kneissl, *Phys. Status solidi B*, 2017, **254**, 1600711.

48 J. Kioseoglou, E. Kalesaki, L. Lymperakis, T. Karakostas and P. Komninou, *J. Phys.: Condens. Matter*, 2012, **25**, 045008.

49 W. Paszkowicz, S. Podsiadło and R. Minikayev, *J. Alloys Compd.*, 2004, **382**, 100–106.

50 W. A. Harrison, *Electronic structure and the properties of solids: the physics of the chemical bond*, Freeman, San Francisco, 1980.